

Yan ZHANG, Yukun ZHU, Yanhua PENG, Xiaolong YANG, Jian LIU, Wei JIAO, Jianqiang YU

Spontaneous polarization enhanced bismuth ferrate photoelectrode: fabrication and boosted photoelectrochemical water splitting property

© Higher Education Press 2021

Abstract In this paper, the fabrication of a highly orientated $\text{Bi}_2\text{Fe}_4\text{O}_9$ (BFO) photoelectrode in the presence of two-dimensional (2D) graphene oxide (GO) was reported. It was found that the GO can be used as a template for controlling the growth of BFO, and the nanoplate composites of BFO/reduced graphene oxide (RGO) with a high orientation can be fabricated. The thickness of the nanoplates became thinner as the ratio of GO increased. As a result, the ferroelectric spontaneous polarization unit arranges itself in the space in a periodic manner, leading to the formation of a polarization field along a special direction. Therefore, the created built-in electric field of the nanoplate composites of BFO/RGO is improved upon the increase of the amount of RGO. As expected, carrier separation is enhanced by the built-in

electric field, therefore substantially enhancing the photoelectrochemical (PEC) activity of water splitting compared to pure BFO under the irradiation of visible-light.

Keywords bismuth ferrate, ferroelectric polarisation, photoelectrochemical (PEC) water splitting, graphene oxide (GO), high orientation

Received May 1, 2021; accepted Jul. 31, 2021; online Sept. 15, 2021

Yan ZHANG, Yukun ZHU, Yanhua PENG, Xiaolong YANG
School of Chemistry and Chemical Engineering, Qingdao University,
Qingdao 266071, China

Jian LIU
State Key Laboratory of Catalysis, Dalian Institute of Chemical Physics,
Chinese Academy of Sciences, Dalian 116023, China

Wei JIAO
Laboratory of Clean Energy Chemistry and Materials, Lanzhou Institute
of Chemical Physics, Chinese Academy of Sciences, Lanzhou 730000,
China

Jianqiang YU (✉)
School of Chemistry and Chemical Engineering, Qingdao University,
Qingdao 266071, China; Laboratory of Clean Energy Chemistry and
Materials, Lanzhou Institute of Chemical Physics, Chinese Academy of
Sciences, Lanzhou 730000, China
E-mail: jianqyu@qdu.edu.cn

Special Issue—Photocatalysis: From Solar Light to Hydrogen Energy
(Guest Editors: Wenfeng SHANGGUAN, Akihiko KUDO, Zhi JIANG,
Yuichi YAMAGUCHI)

1 Introduction

Photoelectrochemical (PEC) water splitting is a promising approach for producing hydrogen and oxygen by using solar energy [1–3]. Since the central part of a PEC cell is the photoelectrode, exploring the photoelectrode materials with a high photo-to-current conversion efficiency has been considered essential for establishing such a system. It has been established that two major limitations to achieve a high efficiency for photocatalytic and PEC conversion are the efficient separation of photogenerated electron-hole (e^-h^+) pairs and the retention of the separated carriers to avoid their recombination.

In recent decades, researchers have developed various strategies to improve the charge carrier separation efficiency of the photocatalysts [4]. The most common strategies include the doping of transition metals, heterojunction fabrication, noble metal modification, surface defect engineering, and so on. However, little progress has been made in bulk charge separation. At present, the influence of a built-in electric field on the photocatalytic performance of materials has become a hot spot of research in the photocatalysis community [5–7]. Recently, polarization field engineering has been demonstrated to be an effective strategy to enhance photocatalytic and PEC performances. The polar unit in polar materials arranged in the space periodically, leads to a polarization field along a

special direction. The polarization field can drive electrons and holes to transfer along the opposite direction, which is beneficial for the separation of e^-h^+ pairs and thus improves the PEC performance [8]. Ferroelectric crystals possess a strong inversion symmetry breaking with a permanent spontaneous electric polarization, which could serve to promote the separation of photoexcited carriers. Consequently, ferroelectrics with an intrinsic built-in electric field could be utilized to boost the PEC properties simply by combining them with traditional semiconductor materials. Since TiO_2 photoelectrodes were first reported in 1972 [1], a variety of novel ferroelectric materials have been exploited as photoelectrode materials (i.e., $BiOIO_3$ [9,10], Bi_2MoO_6 [11], Cu_2O [12,13], Fe_2O_3 [14–17], CdS [18], MoS_2 [19], and $BiVO_4$ [20–22]) for water splitting. Chen et al. reported the recent progresses in charge separation advanced by different types of polarization, such as macroscopic polarization, piezoelectric polarization, ferroelectric polarization, and surface polarization, together with the related mechanisms [23]. This research facilitates the understanding of the role of polarization in photocatalytic materials fabrication. However, most of the studies on polar photocatalysts focus on exploring polar semiconductors as new photocatalysts, while studies on the control of the synthesis of a ferroelectric material so as to modulate the polarization electric field and therefore to enhance the photocatalytic and photochemical properties, as well as the mechanism of charge separation by ferroelectric built-in electric field are rarely reported.

As a typical ferroelectric crystal, bismuth ferrite has been demonstrated to be a promising visible-light-driven photocatalyst due to its narrow band gap and high chemical stability [24,25]. $Bi_2Fe_4O_9$ (BFO) is known as an orthorhombic crystal structure with lattice constants of $a = 7.965 \text{ \AA}$, $b = 8.440 \text{ \AA}$, and $c = 5.994 \text{ \AA}$. Its band-gap is approximately 2.0 eV, which is appropriate for visible-light absorption. In previous works, BFO showed oxidative decomposition over various organic contaminants under visible-light irradiation [26–28]. There are few reports of its PEC performance [29–32]. Meanwhile, because its reactivity is low, it is necessary to improve its PEC performance for further applications. However, the ferroelectrics of these composites come from multiple domains with various polarization directions. The polarization will be switched if an electric field which varies in orientation for different domains is applied. The extra electrode polarizing process is inconvenient and undesirable for catalytic applications. A way to overcome the aforementioned problem of these composite materials is to make the ferroelectric domain the same orientation, which can be implemented by designing a special structure for such ferroelectric semiconductor hybrid photocatalysts.

In this work, a controllable route was developed to synthesize a composite material BFO/ reduced graphene oxide (RGO) hydrothermally under the presence of graphene oxide (GO). Graphene, a single layer two-

dimensional (2D) graphite structure, showed excellent attributes such as unique electronic properties and a large theoretical specific surface area [33]. When the photoelectrode materials form composites with these carbon materials with the conjugative π structure, the recombination of the charge carriers excited by the photoirradiation can be retarded and the photocatalytic efficiency is thus enhanced [34,35].

Compared to pure graphene, GO, however, having a similar layer structure, suffers from a significant loss of conductivity. This problem can be mitigated by partial reduction of the functional groups under hydrothermal treatment [36–38]. The 2D structured GO can work as a template from which the growth of BFO along the surface of GO can be induced, which results in ultra-thin BFO with a highly-oriented structure. On the other hand, the conductivity of the composite materials may be enhanced in the presence of RGO on the surface of BFO, thereby reducing the possibility of recombination of surface charges. Overall, compared with pure BFO, the BFO/RGO composites show enhanced ferroelectric spontaneous polarization and a superior PEC activity toward water splitting.

2 Experimental section

2.1 Sample synthesis

The improved Hummers' method was used to prepare the GO as reported elsewhere [33]. In a typical synthesis route, the BFO/RGO composites were prepared by a hydrothermal process. Typically, the respective ratio of GO ($w(GO) = 0.5\%$, 1.0% , 2.0% , 3.0% , 5.0% respectively, and w is mass fraction) was dispersed in 80 mL of distilled water and sonicated for 1 h. Simultaneously, a bismuth nitrate solution was prepared by dissolving 2 mmol of $Bi(NO_3)_3 \cdot 5H_2O$ into 30 mL of 2.0 mol/L of nitric acid aqueous solution under vigorous stirring. Then, a ferric nitrate solution was prepared by adding 4 mmol of $Fe(NO_3)_3 \cdot 9H_2O$ to the aforementioned solution and dissolved. Afterwards, the above two kinds of solutions were mixed and stirred continuously for 1 h. The coprecipitation process was implemented by dropping slowly the concentrated ammonia into the above mixed solution by which a brown precipitation is formed from the bismuth ions and the iron ions. After stirring for 30 min, the suspension solution was washed with deionised water and ethanol for several times until the NO_3^- ions were removed, leaving only the brown suspended solid. After that, the brown suspended solid was transferred into a 100 mL of Teflonlined autoclave into which, 40 mL of NaOH (10 mol/L) was added slowly. After stirring for 30 min, the autoclave was sealed and kept at 200°C for 12 h. The products were collected by centrifugation and thrice-washed with deionised water to remove soluble

ionic impurities. Then, the samples were dried at 90°C in air. For comparison, the BFO alone was prepared in the absence of GO under the same experimental conditions.

2.2 Characterisations

The crystalline structure of the samples was recorded by X-ray diffraction (XRD) patterns on a DX-2700 using Cu irradiation. The morphologies and microstructures of the prepared samples were further examined with a scanning electron microscope (JSM 6301). The high-resolution transmission electron microscopy (HRTEM, transmission electron microscopy (TEM)) images were obtained with a JEM 2010F field emission transmission electron microscope (An accelerating voltage is 200 kV). The Raman spectra were collected with a LabRam HR 800 apparatus. The optical absorbance spectra of the samples were measured using a UV-visible spectrophotometer (JASCO-550). X-ray photoelectron spectroscopy (XPS) was recorded in a PHI 5300 ESCA system. The X-ray source used was an Al K α with a power of 250 W. The charge effect was calibrated using the binding energy of C 1s.

2.3 Photoelectrode fabrication and PEC measurement

The BFO/RGO film photoanode was prepared by electrophoretic deposition on indium tin oxide (ITO) glass supports. The electrophoretic deposition was conducted in 20 mL of acetone solution containing 10 mg of iodine and 20 mg of photocatalyst powder and dispersed by sonication for 5 min. The addition of iodine produced H⁺ by the reaction with acetone and thus endowed the particles with positive charge. The ITO electrode (1.5 cm \times 4 cm) was immersed in the solution, parallel to the Pt electrode in the solution, and then a 10 V bias was applied between them for 200 s under potentiostat control. After this process was repeated 20 times, the electrode was dried and then calcined at 473 K for 60 min. The exposed effective area of the ITO glass was set to 1.0 cm \times 1.0 cm.

The PEC performance was investigated using a CHI electrochemical workstation (CHI 760C, Shanghai Chenhua, China) in a standard three-electrode cell with a BFO-based electrode, a platinum foil counter electrode, and an Ag/AgCl electrode reference electrode. The working electrodes of BFO and BFO/RGO were fabricated using the electrophoretic deposition method mentioned above. Na₂SO₄ (0.1 mol/L) and Na₂SO₃ (0.1 mol/L) solutions purged with N₂ were the electrolyte. A 300 W Xe illuminator (Peking Changtuo, PLS-SXE300, 150 mW/cm²) with a 420 nm cut-off filter was used as the visible light source. The electrodes were irradiated from the back side (ITO substrate/semiconductor interface). The transient photocurrent-time curves were measured at a 0-V bias potential. The flatband potentials (V_{fb}) were deter-

mined from Mott-Schottky (MS) plots by using the electrochemical method. The MS measurements were performed at a fixed frequency of 1000 Hz with an amplitude of 10 mV, at various applied potentials.

3 Results and discussion

3.1 Morphological and structural characterisations

The morphologies and microstructures of the BFO and BFO/RGO composites were studied by using scanning electron microscopy (SEM) and TEM, respectively. The SEM image in Fig. 1(a) and the TEM image in Fig. 1(c) show that the platelets crystals of BFO are formed with a thickness of 200–600 nm and an edge length ranging from 600 nm to 1.5 μ m. The HRTEM image of the regions is displayed as Fig. 1(e). It can be seen that the (200) lattice fringes with a respective space of 0.39 nm are clearly visible. From the inset in Fig. 1(e), the selected area electron diffraction (SAED) patterns recorded from a single plate (area in the box in Fig. 1(e)), provide clear diffraction spots instead of diffraction rings, suggesting a single crystal nature within the plate. The SAED pattern could be indexed as the expected (200), (220), and (020) reflections in the (001) zone of bulk BFO, which confirms that the top surface of the sheet presents a (001) facet. Interestingly, the addition of GO to the synthesis precursor results in the formation of rhomboidal sheets with a thickness of 50–120 nm and an edge length from 1 μ m to 1.5 μ m, which can be conformed from the lower resolution TEM image. It is evident that the BFO/RGO sheets are much thinner than the pure BFO plates. According to the SAED patterns (see the inset in Fig. 1(f)), the HRTEM image (Fig. 1(f)), and the crystallographic symmetries of BFO [35], the top and bottom of the sheet are recognized respectively as (110) and ($\bar{1}$ 10) facets, while the side of the sheets presents a (001) facet. The sharp diffraction spots in SAED patterns and the clear lattice fringes in the HRTEM image confirm that the BFO sheets have a high crystallinity. In addition, the shape of BFO sheets is not a single plate, probably because of the coexistence of minor facets such as (020) besides (110).

The crystal structures of pure phased BFO and the BFO/RGO with various weight ratios of GO were further analyzed by XRD patterns and illustrated in Fig. 2. All of the diffraction peaks can be assigned to orthorhombic BFO (JCPDS No.25-0090), demonstrating that single-phase BFO samples were obtained. Importantly, by increasing the proportion of GO, (001) facets of BFO/RGO of a higher relative intensity could be observed in the XRD patterns compared to that of pure BFO. This observation suggests that the proportion of (001) facet increases with the amount of GO when the BFO plates transforms into sheets after adding GO into the synthesis precursor. This

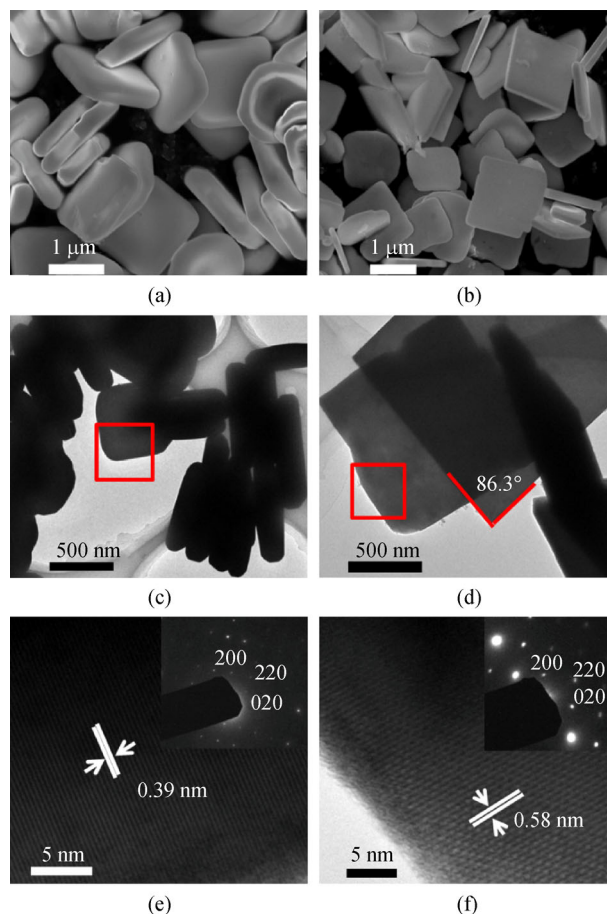


Fig. 1 Typical SEM, TEM, and HRTEM images.

(a) SEM of BFO; (b) SEM of BFO/RGO ($w(\text{GO}) = 2.0\%$); (c) TEM of BFO; (d) TEM of BFO/RGO ($w(\text{GO}) = 2.0\%$); (e) HRTEM of BFO; (f) HRTEM of BFO/RGO ($w(\text{GO}) = 2.0\%$) (The inset in (e) and (f) show the corresponding SAED patterns of the BFO and BFO/RGO sheets, respectively).

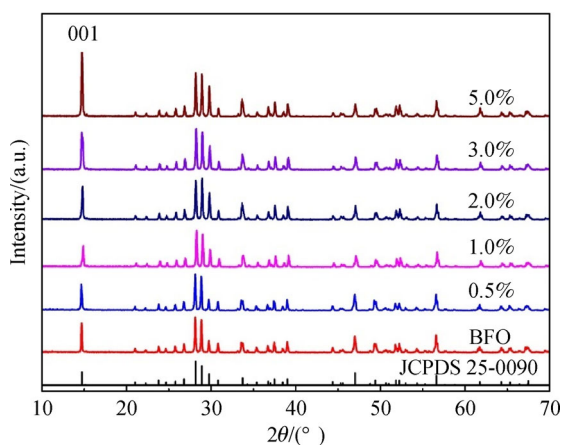


Fig. 2 XRD patterns of BFO, BFO/RGO composites (at a GO mass fraction of 0.5%, 1.0%, 2.0%, 3.0%, and 5.0%, respectively).

result is in agreement with the observations in the SEM and TEM images.

To clarify the substantial role of GO sheets on the BFO/RGO growth, the distribution of RGO on the single BFO/

RGO sheet was investigated by collecting the products at different growth stages and observed by TEM and SEM. The images are exhibited in Fig. 3 and Figs. 4(a)–4(c), respectively. As shown in Figs. 4(a)–4(c), compared to other previous works, during which large sheets of RGO could not be observed, on the contrary, it can be seen that some tiny RGO sheets were coated on the surface, especially at the edge of BFO. The RGO coated on BFO is about 10 nm in thickness, which could be observed in Fig. 3. The whole growth process is summarized in Fig. 4(d).

For the mullite-type structures of BFO, (001) is the most stable facet while (110) and ($\bar{1}10$) have a higher surface energy [36]. This fact indicates intrinsically a faster growth of BFO along (110) or ($\bar{1}10$) than along (001). However, in the presence of GO, the growth rate of (110) facet is retarded due to the coverage of GO. As is known, graphene is a 2D crystalline allotrope of carbon. The carbon atoms that packed in a regular sp^2 -bond are chemically the most reactive. The inorganic Fe^{2+} and Bi_2O_2^+ ions can be easily bonded on the surface of graphene under a certain condition. Therefore, during the hydrothermal growth of

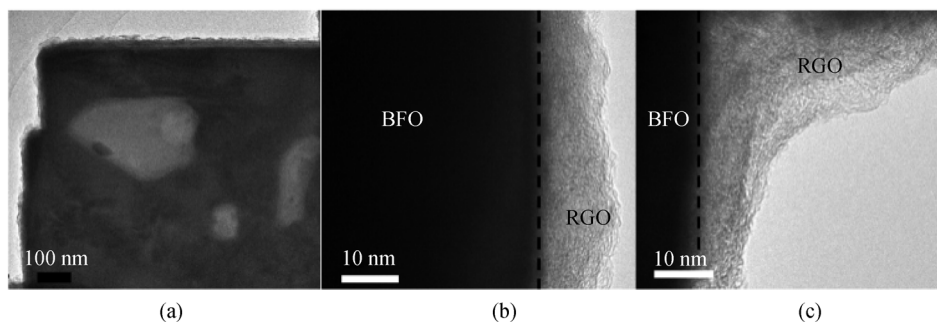


Fig. 3 Typical TEM images of BFO/RGO ($w(\text{GO}) = 2.0\%$).

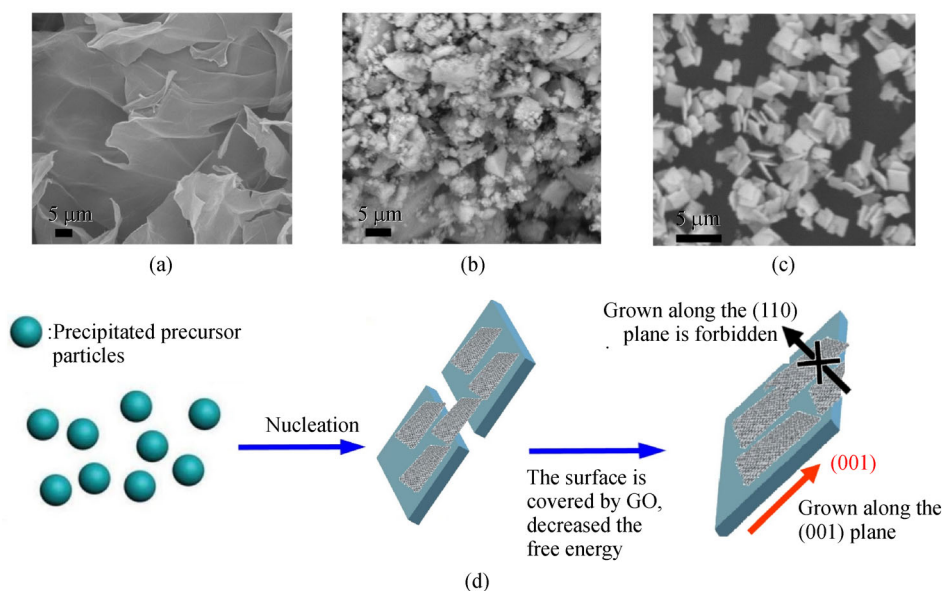


Fig. 4 SEM morphologies of the products in different growth stages.

(a) Pure phased GO; (b) precursor mixture before crystallization; (c) synthesized BFO/RGO sample after crystallization; (d) growth of BFO/RGO.

BFO nanocrystals, the graphene is favorably adsorbed onto the (110) and $(\bar{1}10)$ facets of BFO due to the higher surface energy of these two facets. The “blocking effect” of the graphene restrained the further growth along the direction of these two facets and therefore induced the inorganic ions to preferential growth along the graphene plane orientation. That is to say, the 2D planar structure of GO could work as a template and facilitate the crystallization of composite materials of BFO/RGO with a high orientation.

3.2 PEC water splitting performance

The PEC performances of water splitting over BFO and BFO/RGO photoelectrodes were investigated in a three-electrode PEC cell under visible-light ($\lambda > 420 \text{ nm}$). The working electrodes of the BFO and BFO/RGO films were fabricated by the electrophoretic deposition. The counter electrode used is a platinum foil, and the reference electrode is a Ag/AgCl electrode.

Figure 5 depicts the time-dependent photocurrent

curves of the BFO/RGO composite photoelectrode at various mass fractions of GO. The photocurrent density of the pure phased BFO and BFO/RGO composite photoelectrodes (at a GO mass fraction of 0.5%, 1.0%, 2.0%, 3.0%, and 5.0%, respectively) is 2.7, 8.4, 18.7, 36.3, 27.8, and $14.9 \mu\text{A}/\text{cm}^2$, respectively. As the mass fraction of GO increases, its photocurrent first gradually improves; when the mass fraction is 2.0%, the current density arrives at a maximum value. Then the density continues to decrease with a further increase in the ratio of GO, but the value is still more intensive than the optical current density of pure BFO. The photocurrent density of BFO/RGO ($w(\text{GO}) = 2.0\%$) is about 13.5 times that of the pure BFO.

Due to the extremely high electron mobility of RGO, photogenerated electrons of BFO materials migrate rapidly to RGO, facilitating the separation of photogenerated e^-h^+ pairs. Furthermore, with the thickness of BFO decreasing with the increases of GO addition, the transmission distance of electrons and holes in the bulk phase is shortened, suppressing the combination of photoelectron-hole pairs.

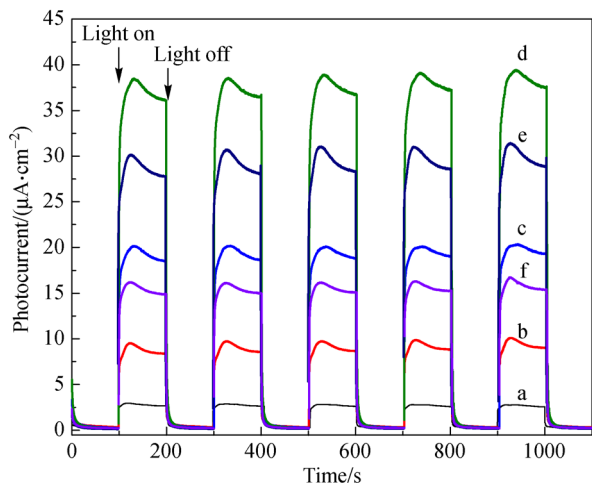


Fig. 5 Photoinduced current densities with time of the BFO/RGO photoanodes under intermittent visible light illumination (a. BFO, b. BFO/RGO ($w(\text{GO}) = 0.5\%$), c. BFO/RGO ($w(\text{GO}) = 1.0\%$), d. BFO/RGO ($w(\text{GO}) = 2.0\%$), e. BFO/RGO ($w(\text{GO}) = 3.0\%$), f. BFO/RGO ($w(\text{GO}) = 5.0\%$), and all curves were obtained at 0 V bias potential).

Therefore, within a certain range, the amount of GO will result in a large current density. However, when the GO content is excessive, light scattering will result in a reduction of the photocurrent density. After five consecutive cycles of open and light, the photocurrent intensity does not change, and the opening and closing light response is rapid, indicating that the composite material is highly stable. For a further verification of the stability of the photoelectrode, the photocurrent density of the BFO and BFO/RGO ($w(\text{GO}) = 2.0\%$) photoelectrodes was investigated at a light opening of 160 min, as manifested in Fig. A1. It can be found that the current density is not attenuate till the light is turned off after 160 min, indicating that the material is stable and no photocorrosion occurs.

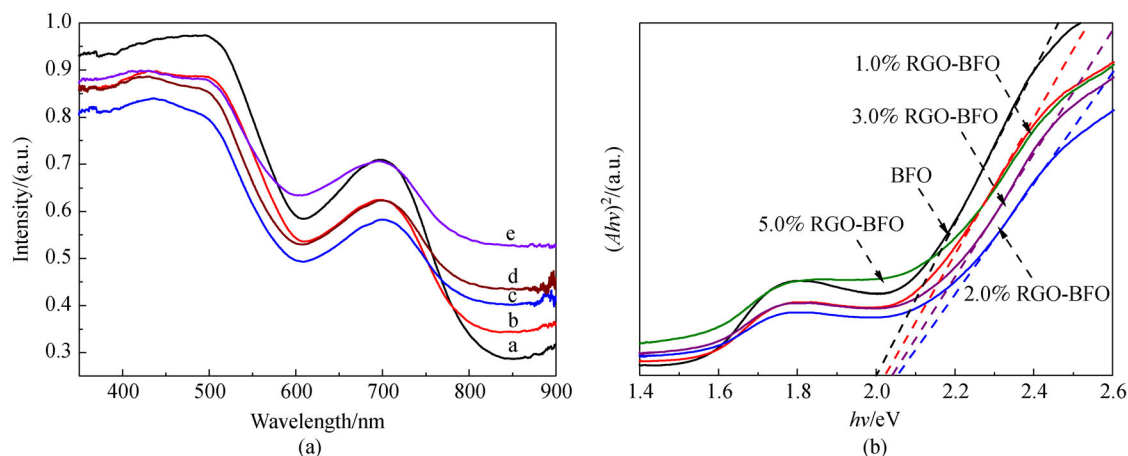


Fig. 6 Photophysical property of BFO and BFO/RGO samples.

(a) UV-Vis absorption spectra; (b) plots of $(Ah\nu)^2$ as a function of photon energy $h\nu$ around the absorption edges (a. BFO, b. BFO/RGO ($w(\text{GO}) = 1.0\%$), c. BFO/RGO ($w(\text{GO}) = 2\%$), d. BFO/RGO ($w(\text{GO}) = 3.0\%$), e. BFO/RGO ($w(\text{GO}) = 5.0\%$)).

3.3 Spontaneous polarization modulation at an enhanced charge separation efficiency

The photophysical properties of the 2D BFO sheets and the BFO/RGO nanocomposites at various mass fraction of GO (at a GO mass fraction of 1.0%, 2.0%, 3.0%, and 5.0%, respectively) were investigated by diffraction reflectance ultraviolet-visible spectroscopy (DRS UV-Vis) which were transformed from the diffuse reflection spectrum according to the Kubelka-Munk theory. Figure 6(a) suggests that all the BFO composites present absorbance from UV to visible light and two absorption edges can be observed at about 610 nm and 850 nm, respectively. It was reported that BFO is a multiband semiconductor [37,38]. The bottom of the conduction band (E_c) and middle narrow bands (E_m) are mainly constituted by the split Fe 3d orbitals, while the top of the valence band (E_v) mainly consists of O 2p orbitals. The two absorption edges are assigned to split Fe 3d transition states, respectively. The two narrow bandgaps indicate that BFO is capable of absorbing solar light, particularly visible light. Figure 6(b) displays the plots of $(Ah\nu)^2$ versus photon energy $h\nu$ around absorbance edges. According to the classical Tauc approach [39], the two bandgaps of BFO nanocrystals are calculated to be 2.00 eV and 1.53 eV, respectively. Compared to pure BFO, the absorbance edges of RGO composite BFO (at a GO mass fraction of 1.0%, 2.0%, 3.0%, and 5.0%, respectively) are 2.06, 2.04, 2.02, and 2.02 eV, respectively. Blue shifts of approximately 0.02–0.06 eV can be clearly observed. This result indicates that the band structures of all BFO/RGO composites have been changed compared to that of pure BFO due to the variation in the anisotropic structure.

For the single-crystal BFO, strongly anisotropic ferroelectric properties can be established due to its layered perovskite structure which consists of interleaved fluorite-like $(\text{Bi}_2\text{O}_2)^{2+}$ layers and FeO_6 octahedra (perovskite slab)

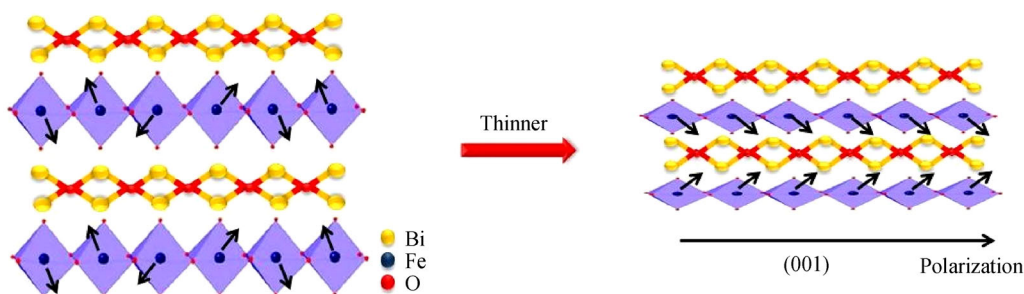


Fig. 7 Schematic diagram of ferroelectric material becoming thinner along the c axis, producing a spontaneous polarization and an enhanced electron transmission performance.

along the c -axis. Therefore, BFO single crystals might exhibit a spontaneous polarization along the c -axis. When the bulk of the ferroelectricity is suppressed mainly along one direction, such as the c -axis, a depolarisation field will be formed. To form an energy-stabilized state, an internal screening in the format of a space-charge region will be formed close to the surface. If the surface is exposed by the $(\text{Bi}_2\text{O}_2)^{2+}$ layers, a positive potential will be produced by the polarization, while the surface exposed by the FeO_6 octahedral structure, a negative potential will be produced by the polarization. Correspondingly, the internal electric fields will be established between the positive potential and the negative potential produced by polarization. The formation of the built-in electrical field and the production of the spontaneous polarization as the thickness of the ferroelectricity is suppressed can be illustrated in Fig. 7.

The polarization effect in ferroelectric materials has been proven to be responsible for the excellent photocatalytic activities. When the BFO/RGO nanosheet exposed with (001) facets are under visible light, photoinduced e^-h^+ pairs are formed and then driven apart by the internal electric fields between the positive potential and the negative potential. Therefore, the separation of photogenerated e^-h^+ pairs along the (001) direction of the BFO/RGO nanosheet will be promoted, and the separation of carriers by the depolarisation fields also inhibits recombination rates, thereby increasing the carrier lifetime, resulting in the observed higher photocatalytic kinetics for the BFO/RGO samples prepared hydrothermally. The benefits of internal electric fields have also been observed by the photo-to-current conversion efficiency measurement. Based on the above analyses, the gradual decrease of the thickness of BFO/RGO samples is beneficial for the photocatalytic kinetics by formatting polarization fields of different intensities. When the charges are transported more efficiently to the surface, and if the charges can be transmitted more quickly to the counter electrode or to the reactive species, the photo-to-current conversion efficiency and the photocatalytic activity will be boosted.

The properties related to charge transport are affected by modifying the amount of RGO on the surface of the BFO,

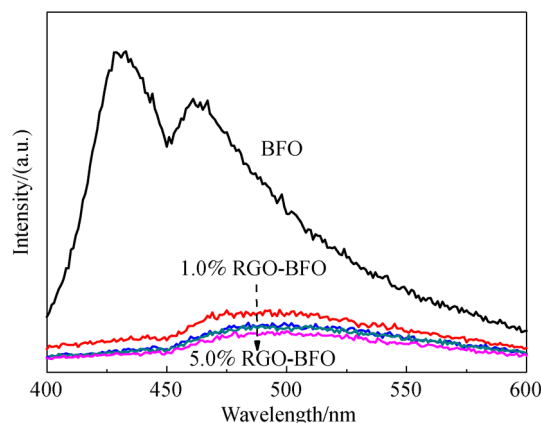


Fig. 8 Photoluminescence spectra of BFO and BFO/RGO composites at various RGO contents.

which can be confirmed by the photoluminescence spectra. As presented in Fig. 8, the intensity of the fluorescence obtained from BFO/RGO is lower than that from BFO. It is established that the modification of RGO on BFO decreases the combination of charge carriers thus giving rise to the superior electronic properties of RGO. Meanwhile, the ultra-thin sheet structure of BFO/RGO has a shorter bulk diffusion length compared to the pure BFO, which is conducive to charge carrier separation. As such, both the electron accepting and transporting properties of graphene in the composite may contribute to the suppression of charge recombination, and therefore improve the photo-to-current conversion efficiency.

The synergistic effects of high polarization on the ultra-thin ferroelectric BFO/RGO nanosheets and the band bending at the interfaces of the heterostructures are considered as the most important factor underlying the enhanced photocurrent response and photocatalytic performance of the BFO/RGO sample. To reveal the mechanism of the enhanced photocurrent response and the improved photocatalytic activity of BFO/RGO, the band-structure properties and ferroelectric properties of the samples were investigated. The band positions including the E_c and the E_v of BFO/RGO, and BFO were examined

by use of an electrochemical impedance technique. Impedance measurements were conducted on photoanodes in 0.1 mol/L Na₂SO₄ electrolyte in the dark to allow construction of MS plots of the BFO and BFO/RGO at various ratios of GO. As shown in Fig. 9, the slopes of the linear part of the curves in the MS plots were positive, showing typical n-type semiconductor characteristics. The E_{fb} (flat band potential, V) and N_D (carrier density, cm⁻³) of the photoanodes in a liquid junction can be estimated from the MS plots according to [40]

$$C^{-2} = (2/(e\epsilon\epsilon_0N_D))[E - E_{fb} - kT/e],$$

where C , e , ϵ , ϵ_0 , E , k , and T represent the capacitance of space charge layers (F/cm²), electron charge (C), dielectric constant, permittivity of vacuum, and applied potential (V), Boltzmann's constant ($1.3806488 \times 10^{-23}$ J/K), and Kelvins temperature (K), respectively.

The E_{fb} of the BFO electrode is determined to be 0.08 V. After loading the RGO, the E_{fb} values of RGO (at a GO mass fraction of 2.0% and 5.0%, respectively) are 0.23 V and 0.12 V, respectively (Table 1). The positive shifts of E_{fb} in BFO/RGO electrodes as compared with the pure BFO electrode are observed.

This result is in agreement with the observations made by the UV-Vis spectra. This suggests that a positive elevation of the Fermi level due to the graphene loading occurs. The elevation of the Fermi level may facilitate the charge separation at the semiconductor/electrolyte interface [42–45]. It is interesting to find that the PEC has a

better water splitting performance if the linked E_{fb} is more positive. It is established that a positive shift in E_{fb} is conducive to the electrons in improving the PEC performance of such BFO/RGO photoelectrodes.

The detailed reason(s) for this result remain unclear, but is possibly a result of the variation in the space charge layer in the presence of RGO that leads to an efficient charge transfer. The carrier density can be calculated by the slope of the MS curves. As the slope of the MS curve decreases, the carrier density of BFO/RGO photoanode also decreases, suggesting a higher carrier density for BFO/RGO photoanodes. An increased value of the N_D in semiconductors increases the charge conductivity, and thus the PEC performance of the photoelectrode. Hence, the increase of carrier density is the main reason for the increase of the carrier density which is the main reason for the increase of photocurrent through the BFO/RGO electrode. However, the slope increases further with the increase of graphene content (5.0%), indicating that the carrier density decreases. This observation is consistent with the result in Fig. 4. Another important role that graphene plays in the BFO/RGO composite is that of an electron acceptor and transporter. First, the reduction of GO to RGO on BFO can be verified by the Raman spectra. Figure 10 displays the Raman spectra of the pure BFO and the BFO/RGO composite. In the Raman spectra of carbon materials, the D band (approximately 1350 cm⁻¹) is associated with the defects in the material while the G band (approximately 1580 cm⁻¹) refers to the existence of an sp^2 carbon-type structures related to the order of the materials. The two characteristic peaks in the spectrum of BFO/RGO are observed at 1330 cm⁻¹ (D) and 1598 cm⁻¹ (G) for the graphite structures, confirming that the GO added to the synthesis precursor of BFO/RGO composites had been reduced to RGO. In contrast, the characteristic peaks are not observed in the Raman spectra of pure BFO.

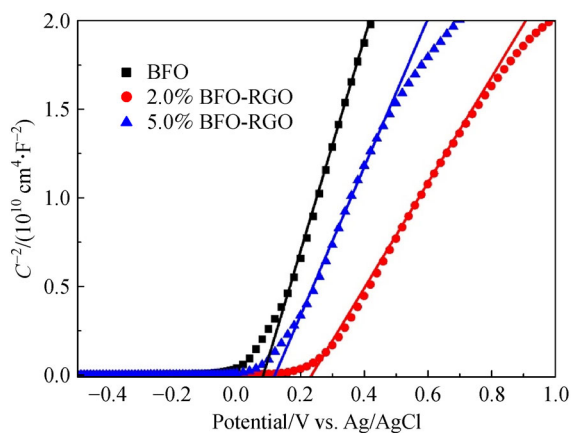


Fig. 9 MS plots of BFO and BFO/RGO photoanodes measured in 0.1 mol/L of Na₂SO₄ (pH 6.3).

Table 1 Flat band potential and curve slope of BFO and BFO/RGO photoelectrodes

Sample	E_{fb}/V	Slope
BFO	0.08	6.31
BFO/RGO ($w(\text{RGO}) = 2.0\%$)	0.23	3.11
BFO/RGO ($w(\text{RGO}) = 5.0\%$)	0.12	4.57

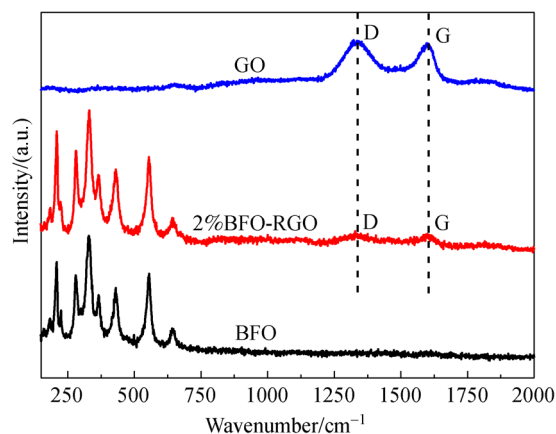


Fig. 10 Raman spectra of BFO and BFO/RGO ($w(\text{GO}) = 2\%$).

4 Conclusions

A novel way of synthesizing BFO/RGO composites by using GO as the template has been developed. As a result, a highly orientated BFO photoelectrode, in the presence of 2D GO, can be fabricated. As such, the ferroelectric spontaneous polarization unit arranges itself spatially and periodically therein, leading to a generation of a polarization field in a certain direction. Therefore, the resulting built-in electric field of the nanoplate composites of BFO/RGO is gradually enhanced upon increasing the RGO content. As expected, the carrier separation is enhanced by the built-in electric field. BFO/RGO composites show a superior photocatalytic activity in PEC water splitting.

Acknowledgements This research was financially supported by the National Natural Science Foundation of China (Grant Nos. 51402314 and 41206067), the Natural Science Foundation of Shandong Province (Grant No. ZR2016BM08), China Postdoctoral Science Foundation (No. 2014M551869), Shandong Excellent Young Scientist Research Award Fund (No. BS2015CL002), and Qingdao Postdoctoral Application Research Fund.

Appendix

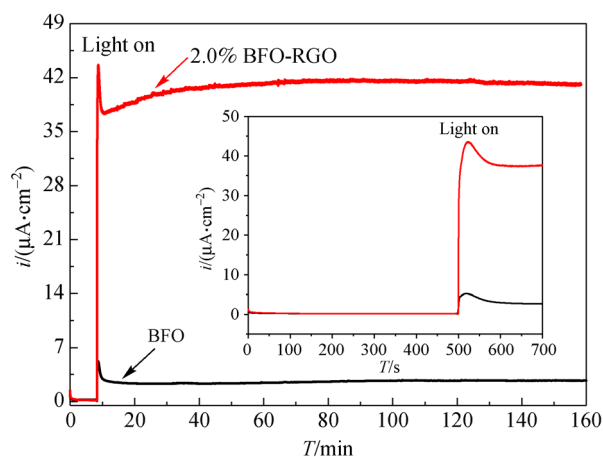


Fig. A1 Photocurrent stability measurement of the $\text{Bi}_2\text{Fe}_4\text{O}_9$ and $\text{Bi}_2\text{Fe}_4\text{O}_9$ -RGO ($w(\text{GO}) = 2.0\%$) photoelectrodes at 0 V bias potential (Insets: photoinduced current densities for the first 700 seconds, and all the curves are measured in 0.1 mol/L Na_2SO_4 + 0.1 mol/L Na_2SO_3).

References

1. Fujishima A, Honda K. Electrochemical photolysis of water at a semiconductor electrode. *Nature*, 1972, 238(5358): 37–38
2. Wang Y, Liu X, Wang X, et al. Metal-organic frameworks based photocatalysts: architecture strategies for efficient solar energy conversion. *Chemical Engineering Journal*, 2021, 419: 129459
3. Chen X, Jin F. Photocatalytic reduction of carbon dioxide by titanium oxide-based semiconductors to produce fuels. *Frontiers in*

4. Energy, 2019, 13(2): 207–220
4. Chen Y, Wang L, Wang W, et al. Enhanced photoelectrochemical properties of ZnO/ZnSe/CdSe/ Cu_{2-x}Se core-shell nanowire arrays fabricated by ion-replacement method. *Applied Catalysis B: Environmental*, 2017, 209: 110–117
5. Ding D, Liu K, He S, et al. Ligand-exchange assisted formation of Au/TiO₂ Schottky contact for visible-light photocatalysis. *Nano Letters*, 2014, 14(11): 6731–6736
6. Ha J W, Ruberu T P A, Han R, et al. Super-resolution mapping of photogenerated electron and hole separation in single metal-semiconductor nanocatalysts. *Journal of the American Chemical Society*, 2014, 136(4): 1398–1408
7. Xiao F, Miao J, Tao H, et al. One-dimensional hybrid nanostructures for heterogeneous photocatalysis and photoelectrocatalysis. *Small*, 2015, 11(18): 2115–2131
8. Fang W, Zhou J, Liu J, et al. Hierarchical structures of single-crystalline anatase TiO₂ nanosheets dominated by {001} facets. *Chemistry (Weinheim an der Bergstrasse, Germany)*, 2011, 17(5): 1423–1427
9. Yang Z, Wan Y, Xiong G, et al. Facile synthesis of ZnFe₂O₄/reduced graphene oxide nanohybrids for enhanced microwave absorption properties. *Materials Research Bulletin*, 2015, 61: 292–297
10. Maletin M, Moshopoulou E G, Kontos A G, et al. Synthesis and structural characterization of in-doped ZnFe₂O₄ nanoparticles. *Journal of the European Ceramic Society*, 2007, 27(13–15): 4391–4394
11. Yang B, Yuan Y, Sharma P, et al. Tuning the energy level offset between donor and acceptor with ferroelectric dipole layers for increased efficiency in bilayer organic photovoltaic cells. *Advanced Materials*, 2012, 24(11): 1455–1460
12. Cui W, Xia Z, Wu S, et al. Controllably interfacing with ferroelectric layer: a strategy for enhancing water oxidation on silicon by surface polarization. *ACS Applied Materials & Interfaces*, 2015, 7(46): 25601–25607
13. Paracchino A, Laporte V, Sivula K, et al. Highly active oxide photocathode for photoelectrochemical water reduction. *Nature Materials*, 2011, 10(6): 456–461
14. Paracchino A, Mathews N, Hisatomi T, et al. Ultrathin films on copper(I) oxide water splitting photocathodes: a study on performance and stability. *Energy & Environmental Science*, 2012, 5(9): 8673
15. Ling Y, Wang G, Reddy J, et al. The influence of oxygen content on the thermal activation of hematite nanowires. *Angewandte Chemie International Edition*, 2012, 51(17): 4074–4079
16. Franking R, Li L, Lukowski M A, Meng F, et al. Facile post-growth doping of nanostructured hematite photoanodes for enhanced photoelectrochemical water oxidation. *Energy & Environmental Science*, 2013, 6(2): 500–512
17. Klahr B, Gimenez S, Fabregat-Santiago F, et al. Photoelectrochemical and impedance spectroscopic investigation of water oxidation with “co-pi”-coated hematite electrodes. *Journal of the American Chemical Society*, 2012, 134(40): 16693–16700
18. Shen R, Ren D, Ding Y, et al. Nanostructured CdS for efficient photocatalytic H₂ evolution: a review. *Science China Materials*, 2020, 63(11): 2153–2188
19. Liang Z, Shen R, Ng Y H, et al. A review on 2D MoS₂ cocatalysts in

- photocatalytic H₂ production. *Journal of Materials Science and Technology*, 2020, 56: 89–121
20. Luo W, Yang Z, Li Z, et al. Solar hydrogen generation from seawater with a modified BiVO₄ photoanode. *Energy & Environmental Science*, 2011, 4(10): 4046
 21. McDonald K J, Choi K S. A new electrochemical synthesis route for a BiOI electrode and its conversion to a highly efficient porous BiVO₄ photoanode for solar water oxidation. *Energy & Environmental Science*, 2012, 5(9): 8553
 22. Luo W, Wang J, Zhao X, et al. Formation energy and photoelectrochemical properties of BiVO₄ after doping at Bi³⁺ or V⁵⁺ sites with higher valence metal ions. *Physical Chemistry Chemical Physics*, 2013, 15(3): 1006–1013
 23. Chen Z, Zhang N, Xu Y. Synthesis of graphene-ZnO nanorod nanocomposites with improved photoactivity and anti-photocorrosion. *CrystEngComm*, 2013, 15(15): 3022–3030
 24. Gao F, Chen X, Yin K, et al. Visible-light photocatalytic properties of weak magnetic BiFeO₃ nanoparticles. *Advanced Materials*, 2007, 19(19): 2889–2892
 25. Papadas I T, Subrahmanyam K S, Kanatzidis M G, et al. Templated assembly of BiFeO₃ nanocrystals into 3D mesoporous networks for catalytic applications. *Nanoscale*, 2015, 7(13): 5737–5743
 26. Ruan Q, Zhang W. Tunable morphology of Bi₂Fe₄O₉ crystals for photocatalytic oxidation. *Journal of Physical Chemistry C*, 2009, 113(10): 4168–4173
 27. Hu Z, Chen B, Lim T T. Single-crystalline Bi₂Fe₄O₉ synthesized by low-temperature co-precipitation: performance as photo- and Fenton catalysts. *RSC Advances*, 2014, 4(53): 27820–27829
 28. Li Y, Zhang Y, Ye W, et al. Photo-to-current response of Bi₂Fe₄O₉ nanocrystals synthesized through a chemical co-precipitation process. *New Journal of Chemistry*, 2012, 36(6): 1297
 29. Poghossian A S, Abovian H V, Avakian P B, et al. Bismuth ferrites: new materials for semiconductor gas sensors. *Sensors and Actuators. B, Chemical*, 1991, 4(3–4): 545–549
 30. Zhang X, Bourgeois L, Yao J, et al. Tuning the morphology of bismuth ferrite nano- and microcrystals: from sheets to fibers. *Small*, 2007, 3(9): 1523–1528
 31. Zhang X, Lv J, Bourgeois L, et al. Formation and photocatalytic properties of bismuth ferrite submicrocrystals with tunable morphologies. *New Journal of Chemistry*, 2011, 35(4): 937
 32. Liu M, Lin C, Gu Y, et al. Oxygen reduction contributing to charge transfer during the first discharge of the CeO₂-Bi₂Fe₄O₉-Li battery: *in situ* X-ray diffraction and X-ray absorption near-edge structure investigation. *Journal of Physical Chemistry C*, 2014, 118(27): 14711–14722
 33. Geim A K. Graphene: status and prospects. *Science*, 2009, 324(5934): 1530–1534
 34. Li X, Yu J, Wageh S, et al. Graphene in photocatalysis: a review. *Small*, 2016, 12(48): 6640–6696
 35. Li X, Shen R, Ma S, et al. Graphene-based heterojunction photocatalysts. *Applied Surface Science*, 2018, 430: 53–107
 36. Wu Y, Luo H, Jiang X, et al. Facile synthesis of magnetic Bi₂₅FeO₄₀/rGO catalyst with efficient photocatalytic performance for phenolic compounds under visible light. *RSC Advances*, 2015, 5(7): 4905–4908
 37. Zhang Y, Zhu Y, Yu J, et al. Enhanced photocatalytic water disinfection properties of Bi₂MoO₆-RGO nanocomposites under visible light irradiation. *Nanoscale*, 2013, 5(14): 6307–6310
 38. Zhou F, Shi R, Zhu Y. Significant enhancement of the visible photocatalytic degradation performances of γ -Bi₂MoO₆ nanoplate by graphene hybridization. *Journal of Molecular Catalysis A Chemical*, 2011, 340(1–2): 77–82
 39. Li X, Yu J, Jaroniec M, et al. Cocatalysts for selective photoreduction of CO₂ into solar fuels. *Chemical Reviews*, 2019, 119(6): 3962–4179
 40. Park H S, Kweon K E, Ye H, et al. Factors in the metal doping of BiVO₄ for improved photoelectrocatalytic activity as studied by scanning electrochemical microscopy and first-principles density-functional calculation. *Journal of Physical Chemistry C*, 2011, 115(36): 17870–17879